

Landslides (2023) 20:1031–1044
 DOI 10.1007/s10346-023-02029-3
 Received: 22 August 2022
 Accepted: 19 January 2023
 Published online: 16 February 2023
 © The Author(s) 2023

Arnaud Watlet  · Hemalatha Thirugnanam · Balmukund Singh · Nitin Kumar M. · Deepak Brahmanandan · Cornelia Inauen · Russell Swift · Phil Meldrum · Sebastian Uhlemann · Paul Wilkinson · Jonathan Chambers · Maneesha Vinodini Ramesh



4D electrical resistivity to monitor unstable slopes in mountainous tropical regions: an example from Munnar, India

Abstract The number of large landslides in India has risen in the recent years, due to an increased occurrence of extreme monsoon rainfall events. There is an urgent need to improve our understanding of moisture-induced landslide dynamics, which vary both spatially and temporally. Geophysical methods provide integrated tools to monitor subsurface hydrological processes in unstable slopes at high spatial resolution. They are complementary to more conventional approaches using networks of point sensors, which can provide high temporal resolution information but are severely limited in terms of spatial resolution. Here, we present and discuss data from an electrical resistivity tomography monitoring system—called PRIME—deployed at the Amrita Landslide Early Warning System (Amrita-LEWS) site located in Munnar in the Western Ghats (Kerala, India). The system monitors changes in electrical resistivity in the subsurface of a landslide-prone slope that directly threatens a local community. The monitoring system provides a 4D resistivity model informing on the moisture dynamics in the subsurface of the slope. Results from a 10-month period spanning from pre-monsoon to the end of the monsoon season 2019 are presented and discussed with regard to the spatial variation of soil moisture. The temporal changes in resistivity within the slope are further investigated through the use of time-series clustering and compared to weather and subsurface pore water pressure data. This study sheds new light on the hydrological processes occurring in the shallow subsurface during the monsoon and potentially leading to slope failure. This geophysical approach aims at better understanding and forecasting slope failure to reduce the risk for the local community, thereby providing a powerful tool to be included in local landslide early warning systems.

Keywords Near surface geophysics · Monitoring · Monsoon · Electrical resistivity tomography · Time-series clustering

Introduction

Moisture-induced landslides are a major hazard in mountainous tropical and subtropical regions. In these regions, seasonal rainfall linked with the monsoon, cyclones or tropical storms, is responsible for the vast majority of landslide events (Froude and Petley 2018). In India, the greatest incidence of moisture-induced landslides occurs during the southwest monsoon, spanning June to September. According to the Global Landslide Catalogue (Kirschbaum et al. 2010, 2015), the southwest monsoon in India accounts for more than 10% of

moisture-induced landslides occurring globally every year. Data by UNISDR also reveals that more than 4.8 million people were affected globally by landslides between 1998 and 2017 (Wallemacq et al. 2018) with India being the most affected country, having more than 56,000 casualties from 4800 landslides between 2004 and 2016 (Froude and Petley 2018). Rapid population growth, unplanned construction in recognised high-risk areas, combined with an increasing rate of extreme climatic events substantially increased the landslide risk in India. Hence, developing effective real-time landslide monitoring is crucial to improve knowledge of slope failure mechanisms, and to build robust landslide early warning systems (LEWS).

Ground-based geophysics has been increasingly used in recent years to help mapping and monitoring unstable slopes (Whiteley et al. 2019). Geophysical imaging approaches are also increasingly recognised as being an important component of local landslide early warning systems (LoLEWS) (Whiteley et al. 2021). A principal benefit of using geophysical methods is that they provide volumetric information on continuous portions of the near surface at the mesoscale, which can bridge the gap between localised borehole information or single-point measurement from sensors and remote sensing techniques. Geophysics is also minimally to non-invasive, which results in much less ground disturbance than traditional, more invasive investigation techniques such as drilling. The use of electrical resistivity tomography (ERT) has proven to be applicable to the characterisation of landslides (Jongmans and Garambois 2007) due to the ability of this technique to image subsurface heterogeneity, lithological variations or geological discontinuities. Building upon the rise of time-lapse ERT experiments, the applicability of ERT monitoring to investigate moisture-induced landslide processes has been highlighted in several studies, such as for imaging moisture build-ups preceding slope instabilities (e.g. Uhlemann et al. 2017) or fissuring processes (e.g. Bièvre et al. 2012). Electrical resistivity is closely linked to moisture content (Telford et al. 1990), which makes it a valuable proxy to monitor moisture-induced landslides. Nevertheless, ERT monitoring has mostly been successfully applied to clay-rich, slow-moving landslides in temperate regions (e.g. Travelletti et al. 2012; Lehmann et al. 2013; Perrone et al. 2014; Holmes et al. 2020; Boyd et al. 2021) or in Alpine environments (e.g. Supper et al. 2014; Gance et al. 2016; Lucas et al. 2017), and, to the best of our knowledge, no successful trial including continuous monitoring has been reported in tropical mountainous regions. In these regions, which have a high landslide susceptibility, such novel monitoring tools could potentially

have a much larger impact in mitigating the risks associated with landslides, but the weather extremes and dispersive soils present a challenging context to deploy ERT monitoring systems.

In this study, we aim to monitor changes in electrical resistivity as a proxy for soil moisture in the shallow subsurface of a slope prone to landslides in the Western Ghats mountain range (India) by investigating the transferability of the method from its application in temperate regions to mountainous tropical regions. We present the deployment of a recently developed ERT monitoring system called PRIME—Proactive Infrastructure Monitoring and Evaluation (Holmes et al. 2020)—at the Amrita Landslide Early Warning System (Amrita-LEWS) site in Kerala, India. The PRIME system is specifically designed as a low-cost and low-power monitoring tool providing near-real-time geophysical imaging, suitable for deployment in remote areas. The Amrita-LEWS site (Ramesh and Vasudevan 2012) is a seasonally reactivated landslide area in the town of Munnar, located in the Western Ghats mountain range, which is one of the most significant landslide-prone areas in India after the Himalaya. This region accounts for large numbers of landslide-related casualties every year (Petley 2012).

In the following sections, we explore the strength of the ERT monitoring system to image slope subsurface moisture dynamics in an area prone to landslides. We present a phased experiment of increasingly developed monitoring over a 2-year period from February 2018 to January 2020, and including a continuous daily ERT dataset spanning from March 2019 to January 2020. We describe the challenges related to the deployment of such a system in a mountainous monsoonal region. We illustrate the applicability of the system in providing 4D imaging of subsurface hydrological processes during the monsoon of 2019. The results are discussed in terms of their hydrological significance and their implications for the understanding of the landslide activity and the development of more informed LoLEWS.

Methodology and site description

Site description

The Amrita-LEWS site is located in Munnar, in the Idukki District of the State of Kerala, South India ($10^{\circ}05'29.6''\text{N}$, $77^{\circ}03'23.3''\text{E}$) (Fig. 1). Munnar is a hill station located in the Western Ghats mountain range at an altitude of ~ 1500 m above sea level. Being of relatively moderate size—with $\sim 32,000$ inhabitants—Munnar is the central tourist spot of the region and attracts increasing numbers of tourists in the area, with recent estimations exceeding 1 million a year (Rajesh et al. 2019). Geomorphologically, the whole region is composed of rugged hills and incised valleys with a structurally controlled drainage network. The area of interest forms part of the Precambrian metamorphic shield of South India and the bedrock at the Amrita-LEWS site mainly consists of pink granite gneiss that has been subject to deep weathering. The weathering intensity is expected to gradually decrease with depth. The weathered bedrock, or saprolite, was reported up to 30 m deep in boreholes logs from the Amrita-LEWS site (Ramesh and Vasudevan 2012).

Rainfall is the main driver of slope failure in the Western Ghats, but the weathering intensity, inappropriate loading and excavation of slopes, insufficient maintenance of drains, unsuitable land use and expanding road network all play an important role in the landslide susceptibility (Kuriakose et al. 2009; Yunus et al. 2021).

Especially, deforestation triggered by the extensive rubber, tea and cardamom plantations has been linked to an increasing number of landslides compared with forested areas in the Western Ghats in general (Kumar and Bhagavanulu 2008) and in the Idukki district in particular (Muraleedharan 2010; Sulal and Archana 2019).

Due to its tropical monsoon climate, Kerala reaches annual rainfall averages above 2800 mm mostly distributed within the wettest 6 months of the year. The main monsoon season, called the southwest (or summer) monsoon, lasts from June to September, with a peak usually falling in July, and accounts for nearly 70% of the annual rainfall. It is quickly followed by the northeast (or winter) monsoon, which peaks in October, is shorter in duration, and has a reduced rainfall intensity. In the pre-monsoon season, from January to May, the precipitation gradually increases to reach averages higher than 600 mm a month in June and July. Recently, the monsoon seasons of 2018, 2019 and 2020 were particularly intense and led to an extremely high number of floods and landslides (Sulal and Archana 2019; Kanungo et al. 2020; Achu et al. 2021).

The south-facing slope of the Amrita-LEWS site itself experienced a massive landslide in 1926 with an estimated volume of 10^5 m³, leaving a large scarp with a concave curvature in the landscape (Ramesh and Vasudevan 2012). A second landslide event occurred in 2005, which was described as a complex rotational slide-debris flow triggered by a torrential downpour (Ramesh and Vasudevan 2012). The monitored slope can be divided in two main domains: above and below the scarp of the 1926 landslide. The top part of the monitoring zone is located in a wooded area, comprising medium-height trees and lemongrass. The soil profile consists of a thin (< 50 cm) layer of brown forest sandy loam (Fig. 1e) on top of the saprolite. In this area, the first horizon of the saprolite consists of a mix of boulders and clasts with preserved bedrock structure within a soil matrix. The bottom part of the slope is still showing the relics of the 1926 landslide event. The vegetation is lighter, with only a few small bushes and lemongrass. The nature of the soil is also different, as the original uppermost horizons slid during the 1926 landslide event. The top soil is extremely thin and consists of coarse-grained, red, sandy silt, on top of the intensely weathered bedrock, which still contains the foliation and the main fabrics of the granite gneiss. In the south-facing slope of the hill, the foliation of exposed weathered bedrock dips steeply to the north, as shown in Fig. 1i. The main identified minerals in the area include quartz, feldspar, biotite and hornblende.

Remnant effects of the latest severe monsoon downpours from 2018 were clearly visible during a field campaign in February 2019, as a few very minor landslides occurred in the steepest parts of the slope (Fig. 1b). In the area directly below the zone where the ERT system is deployed, mass wasting and erosion phenomena occurred including gullies and ravines, and clear evidence of collapsed soil pipes (Fig. 1h). Soil piping is a subsurface erosion process that can occur in the presence of dispersive soils and can interact with mass movement processes by serving as water conduits (Bernatek-Jakiel and Poesen 2018).

The Amrita-LEWS site has been developed as a landslide observatory by Amrita Vishwa Vidyapeetham since 2009, as a response to the 2005 landslide event. The site was chosen due to its strategic location and the strong likelihood of future landslides potentially affecting a community living at the toe of the hill (Ramesh and Vasudevan 2012). Initially, the observatory consisted of a network



Fig. 1 **a** Location of Munnar overlaid on the Indian portion of the landslide susceptibility map by Stanley and Kirschbaum (2017) (image: NASA). **b** General overview of the Amrita-LEWS site, as of February 2019, showing the remnants of past landslide events. **c** Aerial view on the ERT monitoring area highlighting the landslide features and the electrode array. **d** Map of the deployed ERT monitoring system at the

Amrita-LEWS site. Faulty electrodes are marked in light pink (see “ERT acquisition and inversion” section). Capital letters in **c** indicate location of photos in **(e–k)**, which show the soil upslope of the backscarp **(e)**, the slope above the backscarp **(f)**, the coarse ground and ERT cable **(g)**, a collapsed gully **(h)**, a trial pit in the saprolite in the lower part of the slope **(i)**, and the PRIME system **(j, k)**

of sensors installed in the slope, forming one of the world’s first Wireless Sensor Network system for landslide monitoring and early warning (Ramesh and Vasudevan 2012). It was later upgraded to use the Internet of Things (IoT) technology (Thirugnanam et al. 2020). Based on the real-time datasets from the IoT network, site-specific and regional early warnings were issued during the years 2009, 2011, 2013, 2018 and 2019 (Ramesh et al. 2017; Hemalatha et al. 2019). One of the Amrita-LEWS Deep Earth Probe (DEP) boreholes is located within the ERT monitoring area and is equipped with

pore water pressure sensors of which those installed at 10 and 12 m depths collected data overlapping the ERT monitoring period. The Amrita-LEWS site is also equipped with a weather station, which provides rainfall data.

Deployment of the ERT system

At the Amrita-LEWS site in Munnar, the PRIME system has been installed in the centre of the monitored slope in a glass-fibre reinforced

polyester enclosure mounted on a concrete base (Fig. 1j, k). It is powered by 100 W solar panels and 12 V batteries. Results are delivered remotely via a 3G modem, minimising the need for on-site access.

The ERT array consists of four parallel lines making a grid of 128 electrodes with 2 m spacing along the lines and 4 m line separation (Fig. 1d). Each line comprises 32 rod electrodes, which are buried 10 cm below the ground surface, and are connected to the PRIME system through multicore cables.

The ERT monitoring system was deployed in two stages:

- A test phase with the two westernmost lines of the array deployed in November 2017 together with the PRIME system;
- An operational phase starting after installation of the remaining two lines, which were connected to the system in February 2019.

During the test phase, the data quality was not optimal due to relatively poor contact resistances, which define how well the electrodes are galvanically coupled with the surrounding soil material. This was attributed to the nature of the soil, especially in the lower part of the slope, which has a coarse-grained texture that does not favour good coupling due to increased drainage and a lower clay content. This problem was solved by re-deploying the electrodes within a small hole filled with an electrically conductive

graphite aggregate (as seen in Fig. 1h). Comparing the distribution of the contact resistances and reciprocal errors before and after the introduction of the conductive aggregate shows the improvement of the signal (Fig. 2a, b). Electrode positions were surveyed using differential GNSS.

ERT acquisition and inversion

ERT measurements are acquired daily, with a dipole–dipole protocol including reciprocal measurements. Comparing forward and reverse reciprocal measurements is a well-established method for estimating the error associated with the measurements (LaBrecque et al. 1996). The data quality check implies filtering outliers from the data. Readings with either contact resistances higher than 20 kΩ, reciprocal errors higher than 10%, or measured voltages lower than 2 mV are filtered out.

The tropical mountainous environment of the site makes the array of electrodes more vulnerable to being damaged during severe weather conditions. There is potential for the array to become exposed or damaged due to intense soil erosion or the formation of ravines or soil pipes. Wildlife, including pigs and elephants, could also damage the cables or disturb the electrodes. Therefore, special attention is paid to electrodes becoming faulty during the monitoring period. In most

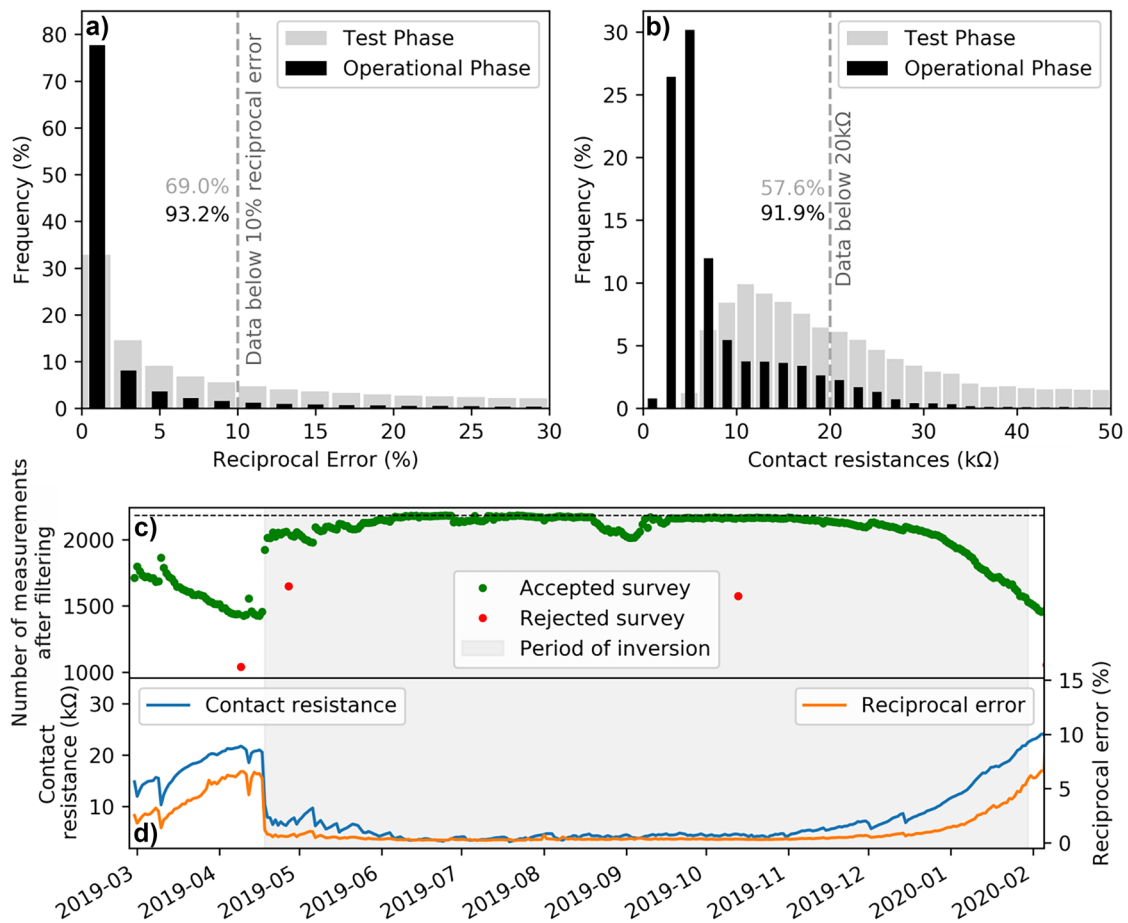


Fig. 2 a Reciprocal error distribution and b contact resistance distribution during the test and operational phases. c Number of measurements per time-step after data filtering. d Temporal evolution of the average contact resistance and reciprocal errors

cases, readings associated with faulty electrodes should be detected during the filtering process. The last electrode of the second line (#64) was damaged during the monsoon season 2018 by the collapse of the soil pipes developing at the toe, after which it was removed from the array. Electrode #70 was also damaged later, after the operational phase began. In both cases, the electrodes exhibited an abrupt occurrence of extremely high contact resistances, clearly indicating that they had been completely disconnected. However, if a damaged or displaced electrode still has sufficient coupling with the soil, it could potentially still take readings, which fall within the designed filter thresholds, but would bias the result of the time-lapse inversion by creating jumps in the time series and artefacts in the resistivity models. To address this issue and to rapidly identify suspicious electrodes, we developed a machine learning approach using unsupervised k-means clustering (Berkhin 2006) of the transfer resistance time series, i.e. the raw ERT data. A series of trends are expected to exist in the transfer resistance data, which result in them being classified in well-defined clusters showing closely related variations. Readings with unphysical transfer resistance variations were rapidly identified by forming a distinct cluster, which could be further scrutinised manually. In our case, this approach allowed the identification of two additional faulty electrodes (#71 and #72). The close proximity of these electrodes with electrode #70, which was already identified as being damaged, makes it likely that the cable was disturbed by wildlife. As a consequence, readings from these three electrodes were removed from the time-lapse dataset as for electrode #64—they are highlighted in light pink in Fig. 1d.

Providing an error model that weights each transfer resistance in the inversion is a crucial step for ensuring reliable results. In this study, we use a reciprocal error model following a multi-bin approach very similar to Mwakanyamale et al. (2012). The reciprocal error is defined as

$$e = |R_n - R_r| \quad (1)$$

where R_n is the forward resistance measurement and R_r is the reverse resistance measurement. As in Slater et al. (2000), the fitted reciprocal error model is expressed as:

$$e = aR + b \quad (2)$$

Here, we adopted a conservative approach consisting in taking an envelope fit of the model, by adding two standard deviation to the mean values of the respective bins, as in Lesparre et al. (2017). This is because the reciprocal errors are closely linked with the contact resistance, and display a bimodal temporal distribution. In the monsoon season, the contact resistance decreases sharply due to the wetting of the soil, which results in low reciprocal errors. In the dry season, the increased contact resistance drives the reciprocal errors up. The envelope fit results in a temporal evolution of the error model which better fits the resistivity time series by increasing more significantly the value of a when the reciprocal error distribution at a given time-step is high, because the standard deviation has also more chance to be higher than in periods with lower average reciprocal error. For all inversions, the reciprocal errors are increased by a constant 3% of the transfer resistance to represent the forward modelling errors, which helped the convergence of the inversion while ensuring smooth spatial and temporal models, in a similar approach as for Boyd et al. (2021).

The 3D time-lapse inversion is carried out using the fully parallelised inversion code E4D (Johnson et al. 2010). Surface topography derived from a UAV photogrammetric survey calibrated with GNSS control points serves as input to generate a 3D mesh for the inversion (see Supplementary Information for more details). The time-lapse inversion uses a smoothness constraint both in space and time. A starting model is computed using a 3D smoothness-constrained inversion of the baseline data. An L2 norm is chosen as the changes in the weathering intensity in the subsurface are expected to be smooth and gradually decreasing with depth. Each time step is then inverted using the baseline as a reference. The time-lapse inversion uses an L2 temporal smoothness constraint—but a relative weight is introduced which removes the constraint for temporal changes lower than a $2 \Omega\text{m}$ threshold, thereby allowing slightly sharper contrasts in resistivity to develop through time and accommodate rapid changes induced by intense rainfall events. A target misfit metric (χ^2) value of 1.0 is assigned to the E4D inversion.

In the time-lapse inversion, the dataset for each time step has to contain the same readings as in the baseline. Rejected readings within the baseline sequence at the following time steps are still included in the inversion but the associated error is set as high as the measurement, which gives a very low weight to the rejected data. In general, a reduced number of measurements in the baseline sequence makes the overall model sensitivity lower. For this reason, and because the number of rejected readings is quite high during most of the dry season, we selected a baseline after the first rain of the pre-monsoon, i.e. 18 April 2019, which resulted in a sharp increase in the data quality. Although this baseline serves as the initial reference in the time-lapse inversion, it does not prevent changes in resistivity being calculated with respect to subsequent time steps, if there is a need to highlight specific processes.

The electrical resistivity is not only sensitive to changes in soil moisture, but also to changes in soil temperature following climatic conditions. However, monthly average temperatures at the site are fairly constant throughout the year, with a maximum amplitude of $2 \text{ }^\circ\text{C}$ between the coldest and the warmest months in average, which would result in $\sim 4\%$ changes in resistivity (Hayley et al. 2007). Therefore, correcting resistivity models for temperature was not considered to be necessary, especially given that the changes in resistivity associated with soil moisture variations are expected to be an order of magnitude higher. Instead, only changes in resistivity higher than 4% are interpreted as being significant. This approach clearly simplifies the post-processing step and reduces the risk of introducing undesired biases in the models given that the thermal parameters of the soil remain unknown in absence of a depth profile of temperature sensors.

Time-series clustering

Applying simple machine learning algorithms to the temporal dataset can help to classify the resistivity models in zones exhibiting relatively similar resistivity dynamics through time (Delforge et al. 2021). The main purpose of these approaches is to highlight landslide domains or potential zones of interest in an independent manner, less influenced by expert-based a priori knowledge. The temporal resistivity evolution of each cluster is then visualised as a separate

time series that is compared to auxiliary data such as rainfall or soil moisture to initiate interpretations on the landslide activity. These outputs can also directly feed in to LoLEWS (Whiteley et al. 2021) with the definition of warning thresholds.

Here, the Hierarchical Agglomerative Clustering (HAC) approach available in the Python library Scikit-learn (Pedregosa et al. 2011) was selected for its additional functionality allowing to include a spatial constraint in the clustering. Details about the HAC method applied in this study are available in the Supplementary Information.

Results

This paper focuses on ERT monitoring results spanning from April 2019 to January 2020, which include the pre-monsoon and the southwest and northeast monsoon periods in June–August and October, respectively. This allows the investigation of the effect of the monsoon on the electrical resistivity distribution in the subsurface of the slope from its onset in April and until the start of the dry season in December.

3D resistivity distribution and material characterisation

The subsurface of the slope is characterised by strong resistivity contrasts, which are likely linked with changes in the soil composition and moisture content, weathering intensity and geological structures. The 3D inversion result for the 18 April 2019 baseline is

shown in Fig. 3. In the upper part of the slope, a superficial layer is associated with very high resistivity values ($> 10,000 \Omega\text{m}$, marker A in Fig. 3b). Such values are explained by the sandy composition of the soil, which has a very low moisture content at the end of the dry season. This superficial layer has irregular extensions at depth, which are attributed to the variable thickness of the soil layer and a spatially variable weathering profile. As seen in Fig. 3a, this high resistivity zone corresponds to a surface area with a lighter vegetation cover, which might indicate a slight variation in the soil composition, possibly due to the weathering of a cluster of quartz veins intersecting the granite gneiss bedrock. These could result in the soil to be locally sandier, thereby having increased electrical resistivities when dry.

The lower part of the slope (marker B in Fig. 3b), south from the scarp of the 1926 landslide, displays low resistivity values ($1000\text{--}2500 \Omega\text{m}$). The material in this area is impacted by the previous large slide and is characterised by a very shallow to exposed weathered bedrock (saprolite), which is marked by lower resistivity values falling in the expected range of resistivity values for a weathered gneiss, as measured in analogue contexts (Jomard et al. 2007). At depth, the average resistivity decreases below $1000 \Omega\text{m}$ (marker C in Fig. 3b), potentially highlighting the saturated bedrock. The water table was recorded at depths of $\sim 16 \text{ m}$ and $\sim 10 \text{ m}$ in the higher part and the lower part of the slope, respectively (Ramesh and Vasudevan 2012). Porewater pressure data from the DEP borehole located in the lower

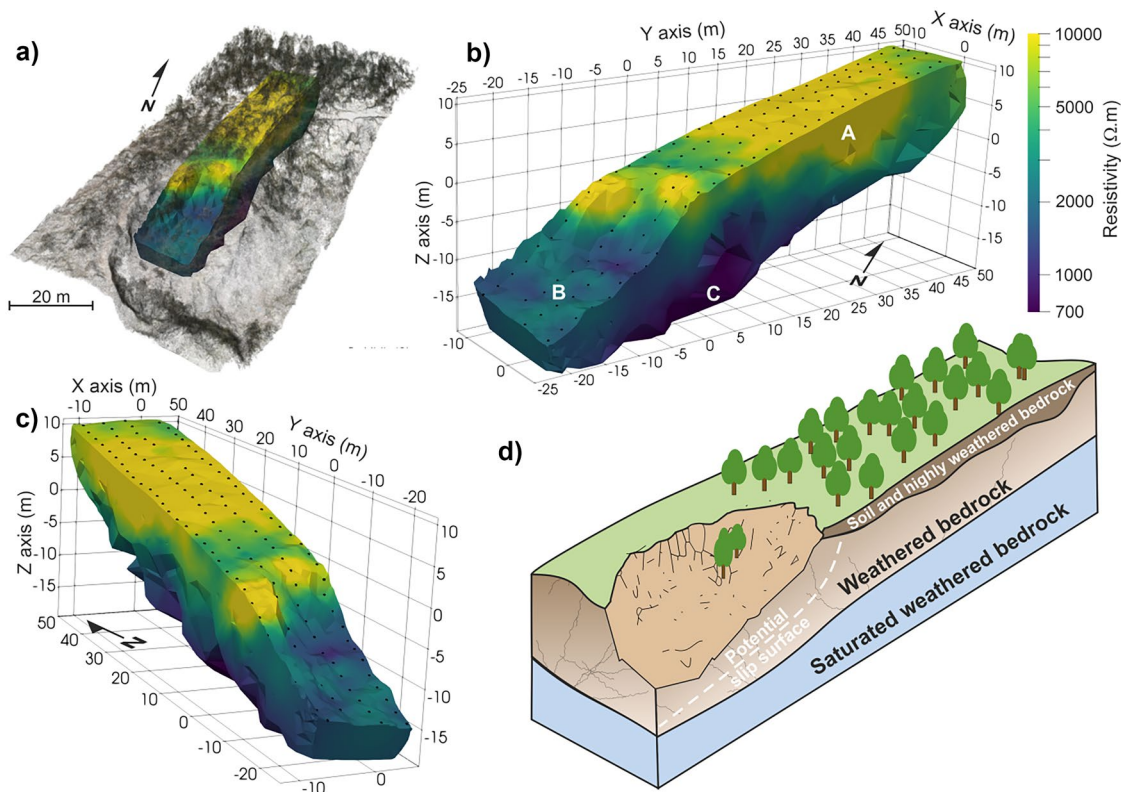


Fig. 3 3D resistivity distribution in the subsurface of the slope as measured on the 18th April 2019. The point cloud from the UAV photoscan used as input to generate the surface topography of the ERT mesh is shown in **a** Black dots in **(b)** and **(c)** represent the location of

the electrodes used in the inversion. Letters in **b** highlight key zones of interests. **d** 3D ground model of the Munnar site derived from the resistivity data and previous studies (Ramesh and Vasudevan 2012)

part of the slope corroborate this information and indicate that the water table is between 10 and 12 m deep.

The crest of the backscarp also appears to be highly resistive, which is likely due to the increased presence of cracks in this zone, which improves drainage and results in drier material. The boundary between the weathered bedrock (in zone B) and less resistive areas near zone C may be an area in which future slip surfaces develop (see Fig. 3).

Resistivity dynamics during the onset of the monsoon

The ERT monitoring system allows investigating the temporal resistivity variations across the 3D model presented in Fig. 3. As mentioned in the “ERT acquisition and inversion” section, the baseline

used in the time-lapse inversion follows the first moderate rain event at the end of the dry season, which occurred on the 18th April 2019, and resulted in a sharp increase of the measured data quality.

First, we investigate the changes in resistivity from the baseline in April and throughout the onset until the peak of the southwest monsoon in August. During this period, the cumulative precipitation rises steadily from April to early July, after which two main periods of intense rainfall occurred. These two periods recorded cumulative precipitation of 322 mm in 6 days with a peak on 19 July and 930 mm in 10 days, with a peak of 330 mm/day on 8 August (Fig. 4a).

Figure 4 displays the decreases in resistivity (i.e. the negative changes in resistivity (%)), in an effort to highlight the processes linked with subsurface re-wetting and moisture build ups. A superficial area in the upper part of the slope is the first to show a slight

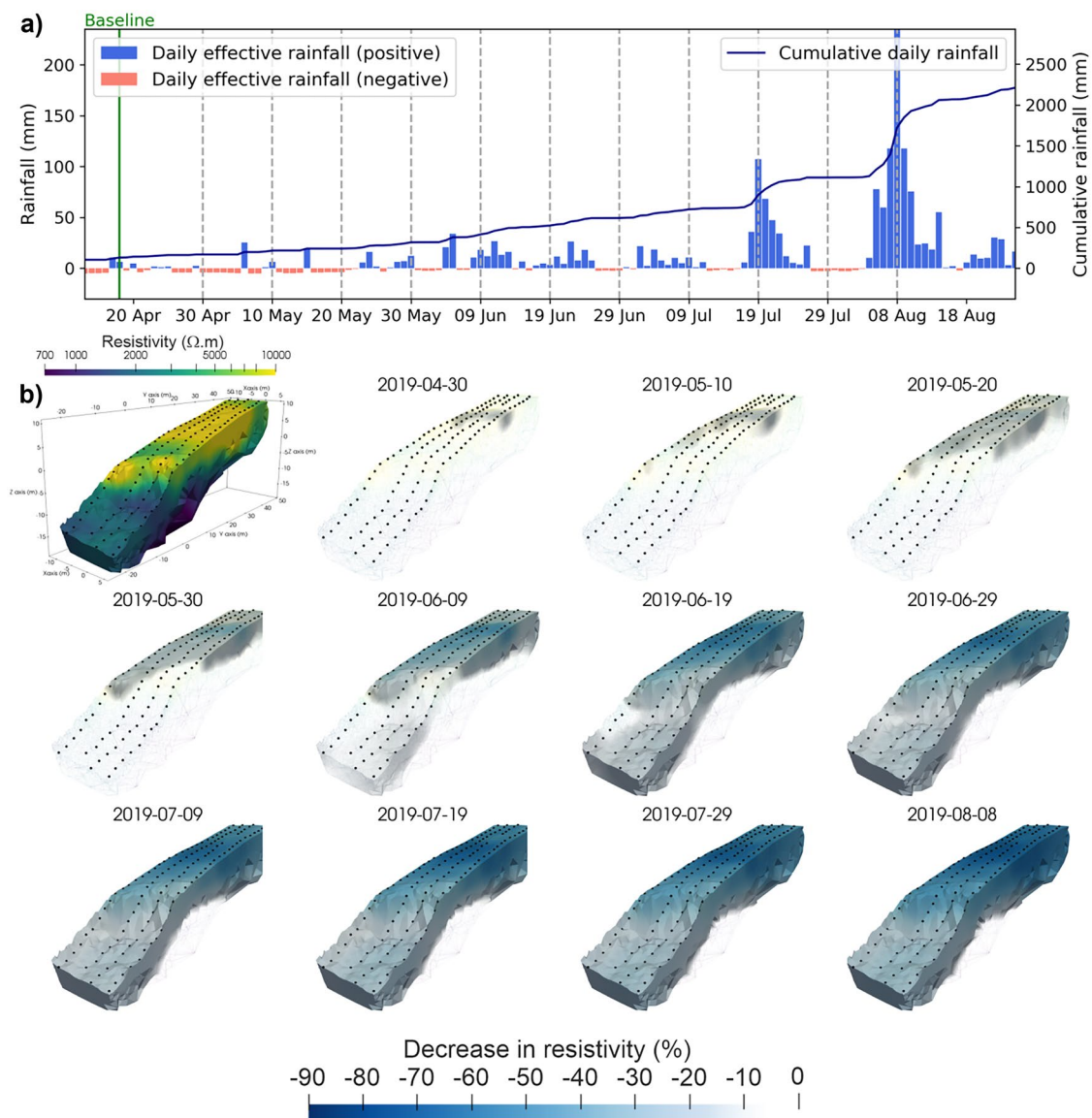


Fig. 4 a Effective rainfall data (i.e. rainfall minus evapotranspiration estimates from the Merra-2 satellite products (Gelaro et al. 2017)). Note that precipitation was measured at 330 mm on 8 August. **b**

Time-lapse resistivity results showing the baseline resistivity distribution (18 April 2019) and decreases in resistivity at regular (10 days) intervals (dashed lines in (a) indicate the dates shown)

decrease in resistivity at the end of April. This area corresponds to the poorly vegetated area exhibiting extremely high resistivity values. This zone of decreased resistivity extends laterally in May and reaches depths of 3–4 m with decreases in resistivity of up to –30%. At this time, the lower part of the slope, below the backscarp, does not show any significant decrease in resistivity. It is only from the beginning of June, when deeper areas (6–8 m depth) are affected by decreases in resistivity, that the resistivity in superficial areas downslope also starts to reduce, albeit less strongly (>–20%) than upslope where decreases of –50% are imaged. Following this and throughout the rest of June and July, the whole slope becomes progressively affected by this continued drop in resistivity down to depths of 10 m. However, the amplitude of the drop

remains higher in the upper part of the slope, with decreases of –90%, whereas downslope of the backscarp, the resistivity does not go below –40%.

Resistivity dynamics following the peak of the monsoon

To be able to image more subtle changes in resistivity during the peak of the southwest monsoon and later, it is more appropriate to use a baseline that is more representative of the resistivity distribution in wetter conditions than in April. Figure 5 displays the changes in resistivity (both negative and positive) as calculated from 15 July, i.e. just before the first peak of the southwest monsoon, and up until the beginning of the dry season in December. During this

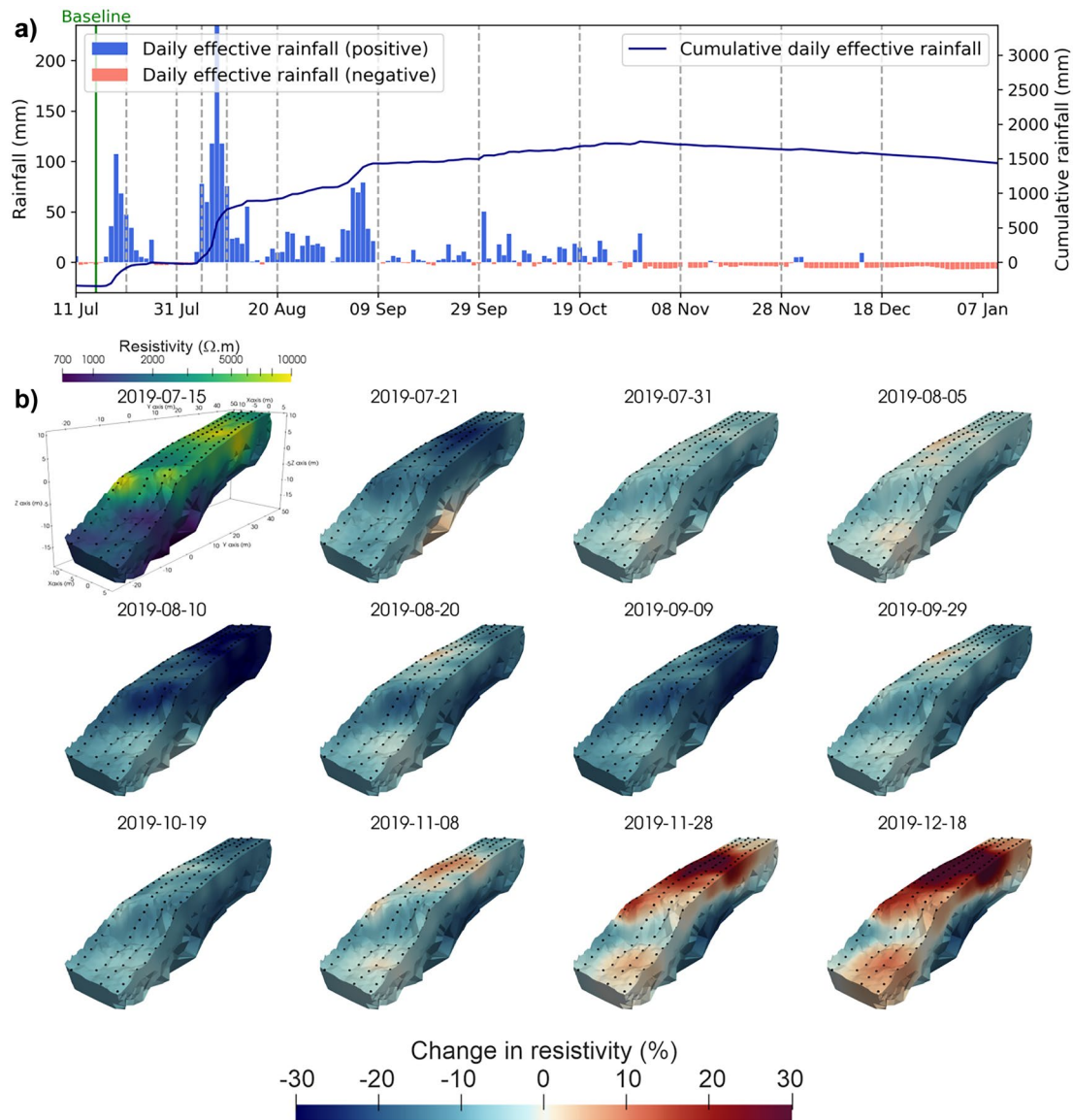


Fig. 5 **a** Effective rainfall data (i.e. rainfall minus evapotranspiration estimates from the Merra-2 satellite products (Gelaro et al. 2017)). Note that precipitation was measured at 330 mm on 8 August. **b** Time-lapse resistivity results showing the baseline resistivity distribution (15 July 2019)

just before the main rainfall periods in the southwest monsoon 2019, and changes in resistivity calculated with respect to the 15 July baseline. Dashed lines in (a) correspond to the time-steps for which the changes in resistivity are shown in (b)

time, three main periods of intense precipitation happened: the two previously mentioned in July and August, as well as another period at the beginning of September, with 363 mm recorded in 7 days. Interestingly, the northeast monsoon was not particularly wet in 2019, with only 16 days of moderate precipitation (10–35 mm/day) recorded in October. These were followed by a long-lasting drought starting in November.

The time-lapse resistivity images presented in Fig. 5b show that the three periods of intense rainfall result in strong decreases in resistivity. As previously observed, the peak of the second episode in August leads to the strongest decrease, which affects zones below the backscarp as much as the upper part of the slope. Between each of these episodes, the resistivity goes up across the slope with more pronounced increases in the upper part of the slope. The resistivity decreases one last time in October, as a consequence of the continued moderate rainfall events. Then, a general increase in resistivity can be observed, starting from the superficial layer upslope, as well as downslope in the south-eastern corner. These areas extend vertically and laterally in November and December. At the same time, the deep part of the resistivity model, which was interpreted as the saturated zone, displays resistivity values lower than in the baseline.

Discussion

Resistivity dynamics linked to hydrological processes

This long-term ERT monitoring experiment is, to the best of our knowledge, the first of its kind to be completed in a mountainous tropical region to image the effect of the monsoon in the subsurface

of a slope prone to landslides. Falae et al. (2021) recently showed the potential of time-lapse ERT in a similar context, at the Pakhi landslide in the Himalayas, by comparing results from two 2D ERT surveys performed before and after the monsoon. With their study, they could identify changes in resistivity linked to spatially variable water seepage, which helped characterise further the structure of the surveyed landslide. The changes in resistivity measured during our experiment at the Amrita-LEWS site have very large amplitudes, which is also undoubtedly linked to the hydrology of the slope. Indeed, only the intense wetting and drying processes occurring in the subsurface of the slope could generate changes in resistivity of such magnitude.

In order to investigate the hydrodynamics of the slope throughout the monsoon, our approach relies on applying time-series clustering (see “Time-series clustering” section) to the 4D resistivity model in order to retrieve clusters representing distinct hydrofacies (i.e. features with distinct hydrological patterns), the resistivity dynamics of which can be analysed further. Figure 6 shows the outputs of the HAC approach with spatial constraints performed on the time series between April 2019 and January 2020. A total of five clusters were selected, after comparing clustering outputs configured to retrieve 2 to 10 clusters. This number was considered optimal, being the best compromise in order for this simplified model not to be overly complex nor too simple, while appropriately representing the subsurface of the slope. As shown in Fig. 6b, these five clusters exhibit average resistivity distributions that are well defined. The multimodal nature of the clusters can be partially explained by the spatial constraint imposed on the clustering, but

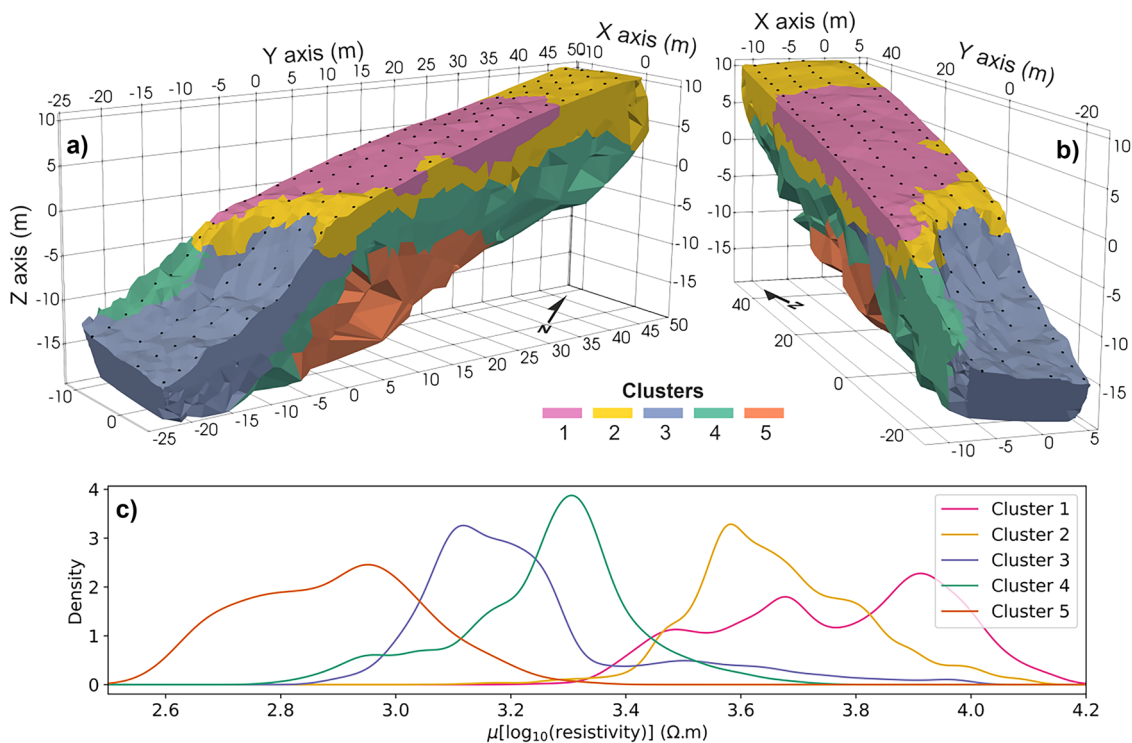


Fig. 6 a, b Results of the clustering using the HAC approach with 5 clusters displayed on the 3D mesh representing distinct features of the landslide. c Average resistivity distribution per cell for each cluster

also by the fact that these clusters contain sub-clusters due to the nested structure of the HAC method.

Cluster 1 aggregates mesh cells at the surface, above the backscarp, overlaying cluster 2, which also includes some portions at the surface both at the top of the northern end of the array and on the crest. Clusters 1 and 2 have an average resistivity between 2500 and 15,000 Ωm . Cluster 3 defines the area downslope of the backscarp with values between 1000 and 2500 Ωm , while cluster 4 contains cells at intermediate depth below the first three clusters, with a peak around 2000 Ωm . Finally, cluster 5 is the deepest cluster defining the most conductive zone with an average value of $\sim 1000 \Omega\text{m}$. The first notable point of the clustering output lies in its good agreement with the material characterisation presented in the “3D resistivity distribution and material characterisation” section, despite some minor discrepancies. For instance, the bottom boundary of cluster 2 does not follow the boundary between the very high resistivity zone (A in Fig. 3) and a layer of intermediate resistivity (on top of C in Fig. 3). This confirms that the similarities in the resistivity dynamics of different cells do not only rely on their average resistivity. Instead, the temporal process leading to changes in resistivity overprints the average resistivity signature, thanks to the z-standardisation (see Eq. 3 in the Supplementary Information) imposed on the resistivity time series before computing the clustering.

It is possible to translate changes in resistivity to changes in moisture content or suction through the use of petrophysical relationships, as was performed on slow-moving landslides in recent studies (Uhlemann et al. 2017; Holmes et al. 2022). These relationships need to be calibrated via laboratory tests on soil samples and are most effective for simple geological contexts, where slope material properties are expected to be fairly homogeneous or clear boundaries exist between different units. In this study, we could not collect a sufficient amount of soil and rock samples to adequately characterise the material properties of the slope and hence develop

reliable petrophysical relationships. The geological context of the site, in which there is gradual weathering intensity with depth, also makes it complex to select appropriate petrophysical parameters. For these reasons, here we only focus on the changes in resistivity as a proxy to infer changes in slope stability parameters (i.e. soil moisture, suction and therefore shear strength).

The temporal evolution of the average resistivity of each cluster is displayed in Fig. 7, and is compared to the effective rainfall and the changes in pore water pressure as measured in the DEP borehole in the lower part of the slope at 10 and 12 m depth. The resistivity dynamics of clusters 1 to 4 can be summarised in three main phases: (i) general decrease during the pre-monsoon, (ii) sustained low resistivity conditions from the end of June to the end of October and (iii) gradual increase in resistivity as the dry season starts. Cluster 5 shows a clear offset with an initial increase in resistivity at the onset of the monsoon while the general decrease occurs in July up until the dry season. For clusters 1 to 4, the magnitude of the decreases in resistivity may seem counterintuitive, with large decreases at the onset of the monsoon and small drops at its peak when soil moisture is expected to be much higher. This is due to the inverse power relationship between bulk electrical resistivity and saturation (Archie 1942; Waxman and Smits 1968; Rhoades et al. 1976), which means that continuous rises in saturation are expected to result in progressively smaller resistivity decreases.

Analysing the dynamics reveals more details of the hydrological processes. Cluster 1 is the first zone to show a reduction in resistivity directly after the baseline in April, closely followed by cluster 2. This can be explained by cluster 1 likely being the sandiest and hence driest part of the slope at the end of the dry season, as evidenced by its extremely high resistivity values, while it is poorly vegetated compared to the surrounding areas (as seen in Fig. 3a), which means that the evapotranspiration is locally reduced and soil moisture builds up more rapidly than in more vegetated areas. It is only at the end of May that cluster 3 shows signs of a significant

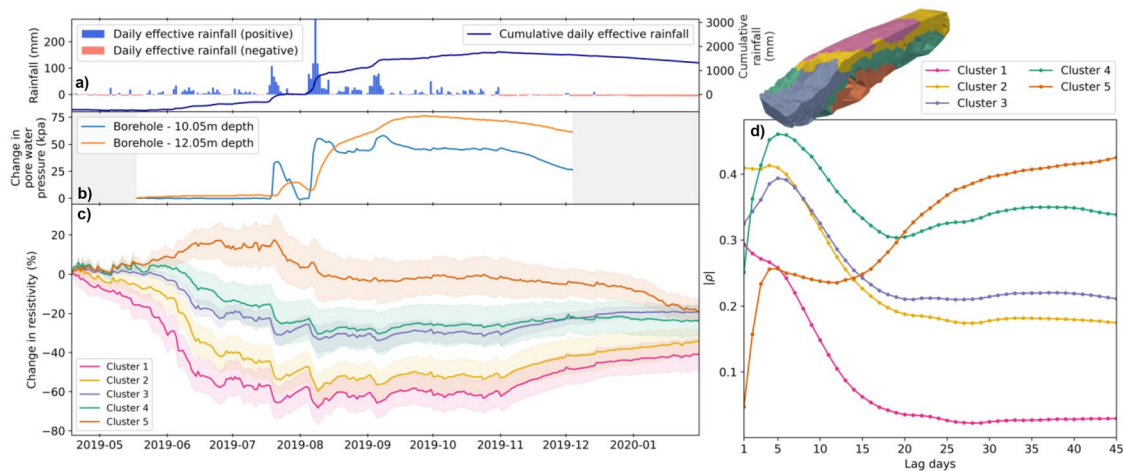


Fig. 7 **a** Effective rainfall data (i.e. rainfall minus evapotranspiration estimates from the Merra-2 satellite products (Gelaro et al. 2017)). Note that precipitation was measured at 330 mm on 8 August. **b** Changes in pore water pressure measured in the DEP borehole. **c** Changes in resistivity with respect to the 18 April 2019 baseline for each cluster.

Standard deviations of each cluster are shown as a transparent filling surrounding each curve. **d** Absolute Pearson correlation coefficient calculated between the cumulative precipitation preceding a time-step t calculated on a number of lag days and the average change in resistivity of each cluster measured over the same period

decrease in resistivity (i.e. $< -10\%$), which means that surface or subsurface runoff processes seem to dominate in the lower part of the slope at the onset of the monsoon. This can be partially explained by the steepest slope angle in this area. The soil pipes discovered at the toe of the slope, just south of the monitoring area, may also enhance drainage, thereby delaying moisture build up.

The wetting front reaches cluster 4, i.e. depths of ~ 5 m, in mid-June as the cumulative rainfall linearly increases, reaching a total of 390 mm from the April baseline. At the same time, the average resistivities of clusters 1 and 2 have changed by -60% and -40% , respectively, while that of cluster 5 still increases slightly. This can only be explained by the fact that the groundwater system is not yet affected by the general wetting of the superficial layers, as corroborated by the lack of variation in pore water pressure measured at depth in the DEP borehole. Then, during the first period of intense precipitation in July with a week-long rainfall event, another reduction in resistivity can be observed for clusters 1–4, directly following the peak of the event on 19 July. It is only at the end of this event, 5 days after the peak, that the first signs of resistivity decrease are recorded in the deeper zone defined by cluster 5. This decrease happens concurrently with the first increase in pore water pressure recorded at 12 m depth, which means that only then the rainwater infiltrates deep enough to actually interact with the groundwater system. Following this period, the superficial layers show a steady increase in resistivity up until the second, more intense period of precipitation in August. This increase is linked to superficial drying processes, likely due to the combined effects of evapotranspiration and gravity driving water infiltration to deeper layers (i.e. cluster 5).

The second rainfall event lasted 10 days and was the most intense recorded in 2019 at the Amrita-LEWS site (see “Results” section) and across the state of Kerala, and resulted in numerous landslides, including in the Idukki district where Munnar was reportedly flooded on the 8 August (Raghnath 2019). Clusters 1 to 3 reach their recorded resistivity minima over the course of the monitoring period on the 9 August, directly following the 8 August rainfall peak of 330 mm. There is a one-day lag because the data presented here are acquired daily between 4:00 and 6:00 am local time, thus most of the rainfall occurred after the ERT measurement on the 8 August. While clusters 1 to 3 experience a steady increase in resistivity at the end of the August rainfall event similar to the previous event in July, clusters 3 and 4 stay relatively stable, which indicates that the moisture in the superficial layer downslope of the backscarp and at intermediate depth remains at a high level, probably close to saturation. The resistivity then reaches another local minimum directly following the third intense rainfall in September. It stays relatively stable after and up until the end of October, when the precipitation stops and a long drought starts, increasing the resistivity of clusters 1 to 4 as these zones progressively dry. Cluster 5 plateaus until the end of December, followed by another small resistivity decrease. The cause of this late decrease could not be investigated further as unfortunately, the pore water pressure sensors installed in the DEP borehole did not provide any data in December 2019 and January 2020. Yet, a potential explanation for this late decrease is linked to a small increase in the water level at depth, potentially following a very slow recharge of the aquifer at the end of the monsoon. Another explanation points to a change in the pore water conductivity, either a seasonal effect or related to the management of the plantation upslope.

Implications for the landslide activity

The resistivity dynamics imaged within the subsurface of the slope provide crucial insights on the potential for the slope to fail. Figure 7d summarises the links between the cumulative precipitation, as aggregated over an increasing number of days, and changes in resistivity computed over moving windows of increasing lengths. For each lag day n , the Pearson correlation coefficient ρ is computed between the cumulative precipitation over n days preceding a resistivity time-step t and changes in resistivity calculated as the difference between day t and day $(t-n)$. As moisture and resistivity are negatively correlated, Fig. 7d displays the absolute correlation coefficient, which helps highlighting that each cluster presents a degree of correlation with the cumulative precipitation. Clusters 1 and 2 have the strongest correlation at 1 day, which means that a rainfall on day $t-1$ has the highest impact on the resistivity on day t . For these clusters, ρ stays stable up until 5 days preceding the resistivity measurement. Conversely, the peak in correlation for clusters 3 and 4 occurs at 5 and 4 days respectively, which highlights that these zones respond differently to rainfall. This is not surprising in the case of cluster 4, which is located at intermediate depths, and therefore, a delay in moisture increase is expected as compared to the surface layer. It is however interesting to examine cluster 3, which comprises cells at the surface of the slope and would be expected to react to rainfall in a similar fashion as clusters 1 and 2. This observation for clusters 3 and 4 is important because it means that loss of suction induced by elevated pore pressure can be delayed after an intense rainfall event. In other words, slope failure could not necessarily occur at the peak of the rainfall event, but rather a few days later under continued precipitation. The deep zone of cluster 5 has a local minimum ρ at 4 days, but a peak correlation at greater than 45 days. This highlights some levels of interaction between surface water and the groundwater system during intense rainfall periods, but in general, the groundwater system, being deeper, is less affected by direct rainwater infiltration.

Most superficial areas of the resistivity model reach their minimum resistivity values of the whole monitoring period following the most intense rain event in August, which indicate that the soil moisture reaches a peak, causing the shear strength to be at a lowest level. A shallow landslide, therefore, becomes more likely to happen. Interestingly, the dynamics of cluster 3 differs from the other superficial clusters 1 and 2, and particularly at the end of the monsoon season (as seen on Figure S1, in the Supplementary Information). While clusters 1, 2 and 4 reach their strongest correlation on 9 August following the peak of the monsoon, it is only after the third intense precipitation period in September, that cluster 3 reaches its minimum resistivity, and thereby its maximum moisture content. This is critical as it means that in this region of the slope (i.e. the backscarp region), moisture levels reach a peak with a significant delay and at a less intense rainfall event (363 mm in 7 days) than the peak event of the monsoon in August (930 mm in 10 days). This has two main explanations: (i) drainage becomes less efficient, or (ii) the pore space has changed to a larger volume, potentially following minor mass wasting processes triggered by the previous rainfall, which emptied some pore spaces previously filled with grains from the rock matrix. Lacerda (2007) identified that saprolitic slopes can fail during a rain period of lower intensity than previous ones

and relates this to a fatigue behaviour of the soils, which undergo repeated pore pressure cycles inducing accumulated shear strains while weakening the intergranular bonds.

In this area, it seems that the soil piping features at the bottom of the slope have also helped to maintain the saturation to a comparably low level in the first months of the monsoon, by enhancing subsurface run-off and drainage, thereby naturally mitigating the decrease of shear strength. However, repetition of intense rainfall periods may have affected these natural conduits, after further collapses of soil pipes or sediment inputs from areas upslope blocking the conduits. As a consequence, the zone may become less drained and pore water pressure may increase more significantly than for previous rainfall events. This, combined with an increase of shear stress in deeper layers as the water table rises, may provide conditions for slope failure to occur.

Two main characteristics can also explain the different behaviour observed between the shallow areas defined by clusters 1 and 2 on one side and cluster 3 on the other side: slope angle and material type. The increased slope angle in the backscarp region results in greater surface run-off than for the area at the top of the slope, potentially resulting in a delayed infiltration. The material in the backscarp region is also likely to have a lower permeability than the shallow layers in the region above the scarp due to it being relatively recently exposed and sitting within a different part of the bedrock weathering profile.

Implication of the ERT monitoring for LoLEWS

The importance of looking at subsurface conditions rather than relying on rainfall data only is being increasingly considered to develop more-informed LoLEWS (Bogaard and Greco 2018; Segoni et al. 2018; Whiteley et al. 2021), which may greatly help in mitigating the landslide hazard in India and globally. For instance, Abraham et al. (2021) investigated the combined use of rainfall and antecedent soil moisture to set up a LEWS in the Idukki district, in which Munnar is located. Marino et al. (2020) have also shown how analysing soil moisture variations can improve the efficiency of LoLEWS by reducing the number of false alarms.

Geophysical measurements provide subsurface data at great spatial and temporal resolution, which can directly feed in to landslide modelling and forecasting approaches. They are therefore perfectly suited to improve LoLEWS (Whiteley et al. 2021). This study validates the applicability of ERT to monitor unstable slopes in a mountainous tropical environment subject to monsoon and demonstrates the added value of the technique for LoLEWS, as it provides an enhanced spatial resolution to conventional monitoring at point locations within the slope. The electrical properties only provide a proxy of slope stability parameters, and seeking to translate the change in resistivity in terms of soil moisture is a complex problem given the inhomogeneous ground properties. Nonetheless, the clustering approach presented in this study demonstrates that the slope hosts non-uniform hydrological processes throughout the monsoon season. This highlights the importance of taking into account the geometry and material distribution within the slope, as well as including ground condition data rather than rainfall data only, when developing early warning systems at the local scale based on the definition of thresholds. 4D time-lapse ERT

is able to provide both the spatial variability and ground condition information, using resistivity as a proxy for soil moisture.

In a LoLEWS context, this monitoring experiment could constitute a baseline in which no significant movement was observed despite severe precipitation. One can hypothesise that the observed hydrodynamics were not of a level to induce failure. However, as monitoring continues it will be important to determine whether the magnitude of changes exceeds the baseline, which might indicate that the slope is moving into an unknown regime where failure might occur. From this, we could start developing an understanding of the range of subsurface conditions over which we expect the slope to be stable. And eventually, rainfall/soil moisture conditions might be linked to actual failure allowing failure thresholds to be defined. Developing a hydro-geomechanical model based on the structure of the landslide revealed by the geophysics will also help calibrating and testing scenarios to build up threshold conditions.

Conclusions

PRIME, an autonomous geophysical system designed for remote monitoring, was deployed at the Amrita-LEWS site in Munnar (Kerala, India), in order to investigate the applicability of ERT to monitor unstable slopes in mountainous tropical regions. The geophysical system collected data on a daily basis during a 10-month period including the monsoon season of 2019. First, the subsurface was characterised using a 3D resistivity model, which shows clear contrasts in resistivity between (i) the soil and highly weathered bedrock (or saprolite), (ii) less weathered portions of the bedrock, including outcropping areas below the scarp of a previous landslide event, and (iii) the saturated bedrock at depth. Then, changes in resistivity induced by moisture building up in the subsurface of the slope could be successfully imaged, thereby providing a 4D resistivity model of the monitored slope to aid understanding water infiltration processes induced by the monsoon. The use of time-series clustering on the electrical resistivity model allowed the retrieval of clusters showing similar resistivity dynamics over time. Five clusters were selected as adequately describing the temporal evolution of subsurface resistivity, and were used to analyse the hydrological response of the slope during the monsoon in more detail and to inform on the evolution of parameters driving the slope stability.

The near-real-time aspect of the ERT monitoring combined with its high spatial and temporal resolution makes it ideally suited for integration with LoLEWS. Volumetric monitoring of the subsurface combined with the definition of thresholds using resistivity as a proxy for slope stability parameters, such as soil moisture, suction and shear strength, clearly has the potential to improve the robustness of LEWS through tracking subsurface moisture dynamics from the ground surface to depth, while adequately accounting for spatial heterogeneity. This study demonstrates that the use of ERT as a monitoring method can be successful in mountainous tropical regions, which paves the way for it to be applied more broadly on targeted sites in India and beyond, thereby contributing to landslide hazard mitigation in the regions where it is most needed. Case studies from other, potentially even more challenging sites such as in the Himalayas, could help in developing more resilient monitoring strategies and validate the technique further as a means to monitor slope stability during the monsoon. Areas of research also include ways to define robust thresholds on outputs of time-lapse

clustering and effectively integrate these in LoLEWS, which will require actual slope failure to be monitored.

Acknowledgements

The authors wish to thank S. Kumar for maintaining the Amrita-LEWS site throughout the duration of this experiment, as well as members of the landslide team at Amrita WNA, and members of Shallow Geophysics at BGS.

Funding

This research project was supported by the British Geological Survey NC-ODA grant NE/R000069/1: Geoscience for Sustainable Futures.

Data availability

Data will be made available on request.

Declarations

Consent for publication The BGS authors publish with the permission of the Executive Director of the British Geological Survey.

Competing interests The authors declare no competing interests.

Open Access This article is licensed under a Creative Commons Attribution 4.0 International License, which permits use, sharing, adaptation, distribution and reproduction in any medium or format, as long as you give appropriate credit to the original author(s) and the source, provide a link to the Creative Commons licence, and indicate if changes were made. The images or other third party material in this article are included in the article's Creative Commons licence, unless indicated otherwise in a credit line to the material. If material is not included in the article's Creative Commons licence and your intended use is not permitted by statutory regulation or exceeds the permitted use, you will need to obtain permission directly from the copyright holder. To view a copy of this licence, visit <http://creativecommons.org/licenses/by/4.0/>.

References

Abraham MT, Satyam N, Rosi A et al (2021) Usage of antecedent soil moisture for improving the performance of rainfall thresholds for landslide early warning. *CATENA* 200:105147

Achu AL, Joseph S, Aju CD, Mathai J (2021) Preliminary analysis of a catastrophic landslide event on 6 August 2020 at Pettimudi, Kerala State, India. *Landslides* 18:1459–1463

Archie GE (1942) The electrical resistivity log as an aid in determining some reservoir characteristics. *Trans AIME* 146:54–62

Berkhin P (2006) A survey of clustering data mining techniques. In: *Grouping multidimensional data*. Springer, pp 25–71

Bernatek-Jakiel A, Poesen J (2018) Subsurface erosion by soil piping: significance and research needs. *Earth-Sci Rev* 185:1107–1128

Bièvre G, Jongmans D, Winiarski T, Zumbo V (2012) Application of geophysical measurements for assessing the role of fissures in water infiltration within a clay landslide (Trièves area, French Alps). *Hydrol Process* 26:2128–2142

Bogaard T, Greco R (2018) Invited perspectives: hydrological perspectives on precipitation intensity-duration thresholds for landslide initiation: proposing hydro-meteorological thresholds. *Nat Hazards Earth Syst Sci* 18:31–39

Boyd J, Chambers J, Wilkinson P, et al (2021) A linked geomorphological and geophysical modelling methodology applied to an active landslide. *Landslides* 1–16

Delforge D, Watlet A, Kaufmann O et al (2021) Time-series clustering approaches for subsurface zonation and hydrofacies detection using a real time-lapse electrical resistivity dataset. *J Appl Geophys* 184:104203

Falae PO, Dash RK, Kanungo DP, Chauhan PKS (2021) Interpretation on water seepage and degree of weathering in a landslide based on pre- and post-monsoon electrical resistivity tomography. *Surf Geophys* 19:315–333

Froude MJ, Petley DN (2018) Global fatal landslide occurrence from 2004 to 2016. *Nat Hazards Earth Syst Sci* 18:2161–2181

Gance J, Malet J-P, Supper R et al (2016) Permanent electrical resistivity measurements for monitoring water circulation in clayey landslides. *J Appl Geophys* 126:98–115. <https://doi.org/10.1016/j.jappgeo.2016.01.011>

Gelaro R, McCarty W, Suárez MJ et al (2017) The modern-era retrospective analysis for research and applications, version 2 (MERRA-2). *J Clim* 30:5419–5454

Hayley K, Bentley LR, Gharibi M, Nightingale M (2007) Low temperature dependence of electrical resistivity: implications for near surface geophysical monitoring. *Geophys Res Lett* 34:L18402. <https://doi.org/10.1029/2007GL031124>

Hemalatha T, Ramesh MV, Rangan VP (2019) Effective and accelerated forewarning of landslides using wireless sensor networks and machine learning. *IEEE Sens J* 19:9964–9975

Holmes J, Chambers J, Meldrum P et al (2020) Four-dimensional electrical resistivity tomography for continuous, near-real-time monitoring of a landslide affecting transport infrastructure in British Columbia, Canada. *Surf Geophys*

Holmes J, Chambers J, Wilkinson P et al (2022) Application of petrophysical relationships to electrical resistivity models for assessing the stability of a landslide in British Columbia, Canada. *Eng Geol* 106613

Johnson TC, Versteeg RJ, Ward A et al (2010) Improved hydrogeophysical characterization and monitoring through parallel modeling and inversion of time-domain resistivity and induced-polarization data. *Geophysics* 75:WA27–WA41

Jomard H, Lebourg T, Tric E (2007) Identification of the gravitational boundary in weathered gneiss by geophysical survey: La Clapière landslide (France). *J Appl Geophys* 62:47–57

Jongmans D, Garambois S (2007) Geophysical investigation of landslides: a review. *Bull Société Géologique Fr* 178:101–112

Kanungo DP, Singh R, Dash RK (2020) Field observations and lessons learnt from the 2018 landslide disasters in Idukki District, Kerala, India. *Curr Sci* 119:1797

Kirschbaum D, Stanley T, Zhou Y (2015) Spatial and temporal analysis of a global landslide catalog. *Geomorphology* 249:4–15

Kirschbaum DB, Adler R, Hong Y et al (2010) A global landslide catalog for hazard applications: method, results, and limitations. *Nat Hazards* 52:561–575

Kumar SV, Bhagavanulu DVS (2008) Effect of deforestation on landslides in Nilgiris district—a case study. *J Indian Soc Remote Sens* 36:105–108

Kuriakose SL, Sankar G, Muraleedharan C (2009) History of landslide susceptibility and a chorology of landslide-prone areas in the Western Ghats of Kerala, India. *Environ Geol* 57:1553–1568

LaBrecque DJ, Miletto M, Daily W et al (1996) The effects of noise on Occam's inversion of resistivity tomography data

Lacerda WA (2007) Landslide initiation in saprolite and colluvium in southern Brazil: field and laboratory observations. *Geomorphology* 87:104–119

Lehmann P, Gambazzi F, Suski B et al (2013) Evolution of soil wetting patterns preceding a hydrologically induced landslide inferred from electrical resistivity survey and point measurements of volumetric water content and pore water pressure. *Water Resour Res* 49:7992–8004

Lesparre N, Nguyen F, Kemna A et al (2017) A new approach for time-lapse data weighting in electrical resistivity tomography. *Geophysics* 82:E325–E333

Lucas DR, Fankhauser K, Springman SM (2017) Application of geotechnical and geophysical field measurements in an active alpine environment. *Eng Geol* 219:32–51

- Marino P, Peres DJ, Cancelliere A et al (2020) Soil moisture information can improve shallow landslide forecasting using the hydrometeorological threshold approach. *Landslides* 17:2041–2054
- Muraleedharan C (2010) Landslide hazard zonation on meso-scale for Munnar, Devikulam Taluk, Idukki District, Kerala. Geological Survey of India, Government of India, New Delhi
- Mwakanyamale K, Slater L, Binley A, Ntarlagiannis D (2012) Lithologic imaging using complex conductivity: lessons learned from the Hanford 300 Area. *Geophysics* 77:E397–E409
- Pedregosa F, Varoquaux G, Gramfort A et al (2011) Scikit-learn: machine learning in python. *J Mach Learn Res* 12:2825–2830
- Perrone A, Lapenna V, Piscitelli S (2014) Electrical resistivity tomography technique for landslide investigation: a review. *Earth-Sci Rev* 135:65–82. <https://doi.org/10.1016/j.earscirev.2014.04.002>
- Petley D (2012) Global patterns of loss of life from landslides. *Geology* 40:927–930
- Raghunath A (2019) Heavy rains and landslides in Kerala kill eight. *Deccan Her.*
- Rajesh CG, Sajini GK, Rethesh SR (2019) Kerala Tourism Statistics 2019. Government of Kerala Department of Tourism, Thiruvananthapuram, Kerala, India
- Ramesh MV, Pullarkatt D, Geethu TH, Rangan PV (2017) Wireless sensor networks for early warning of landslides: experiences from a decade long deployment. In: *Workshop on world landslide forum*. Springer, pp 41–50
- Ramesh MV, Vasudevan N (2012) The deployment of deep-earth sensor probes for landslide detection. *Landslides* 9:457–474. <https://doi.org/10.1007/s10346-011-0300-x>
- Rhoades JD, Raats PAC, Prather RJ (1976) Effects of liquid-phase electrical conductivity, water content, and surface conductivity on bulk soil electrical conductivity. *Soil Sci Soc Am J* 40:651–655
- Segoni S, Rosi A, Lagomarsino D et al (2018) Brief communication: using averaged soil moisture estimates to improve the performances of a regional-scale landslide early warning system. *Nat Hazards Earth Syst Sci* 18:807–812
- Slater L, Binley AM, Daily W, Johnson R (2000) Cross-hole electrical imaging of a controlled saline tracer injection. *J Appl Geophys* 44:85–102
- Stanley T, Kirschbaum DB (2017) A heuristic approach to global landslide susceptibility mapping. *Nat Hazards* 87:145–164
- Sulal NL, Archana KG (2019) Note on post disaster studies for landslides occurred in june 2018 at Idukki District, Kerala. *Geol Surv India Thiruvananthapuram*
- Supper R, Ottowitz D, Jochum B, Kim JH, Römer A, Baron I, Pfeiler S, Lovisolo M, Gruber S, Vecchiotti F (2014) Geoelectrical monitoring: an innovative method to supplement landslide surveillance and early warning. *Surf Geophys* 12:133–150. <https://doi.org/10.3997/1873-0604.2013060>
- Telford WM, Geldart LP, Sheriff RE (1990) *Applied geophysics*. Cambridge University Press
- Thirugnanam H, Ramesh MV, Rangan VP (2020) Enhancing the reliability of landslide early warning systems by machine learning. *Landslides* 17:2231–2246
- Travelletti J, Sailhac P, Malet J-P et al (2012) Hydrological response of weathered clay-shale slopes: water infiltration monitoring with time-lapse electrical resistivity tomography. *Hydrol Process* 26:2106–2119. <https://doi.org/10.1002/hyp.7983>
- Uhlemann S, Chambers J, Wilkinson P et al (2017) Four-dimensional imaging of moisture dynamics during landslide reactivation. *J Geophys Res Earth Surf* 122:398–418. <https://doi.org/10.1002/2016JF003983>
- Wallemacq P, Below R, McLean D (2018) UNISDR and CRED report: economic losses, poverty & disasters (1998–2017). CRED Bruss
- Waxman MH, Smits LJM (1968) Electrical conductivities in oil-bearing shaly sands. *Soc Pet Eng J* 8:107–122
- Whiteley JS, Chambers JE, Uhlemann S et al (2019) Geophysical monitoring of moisture-induced landslides: a review. *Rev Geophys* 57:106–145
- Whiteley JS, Watlet A, Kendall JM, Chambers JE (2021) Brief communication: the role of geophysical imaging in local landslide early warning systems. *Nat Hazards Earth Syst Sci Discuss* 1–13
- Yunus AP, Fan X, Subramanian SS et al (2021) Unraveling the drivers of intensified landslide regimes in Western Ghats. *India Sci Total Environ* 770:145357

Supplementary Information The online version contains supplementary material available at <https://doi.org/10.1007/s10346-023-02029-3>.

Arnaud Watlet (✉) · **Russell Swift** · **Phil Meldrum** · **Paul Wilkinson** · **Jonathan Chambers**

Shallow Geohazards and Earth Observation, British Geological Survey, Nottingham, UK
Email: arnw@bgs.ac.uk

Arnaud Watlet
Geology and Applied Geology Unit, Faculty of Engineering, University of Mons, Mons, Belgium

Hemalatha Thirugnanam · **Balmukund Singh** · **Nitin Kumar M.** · **Deepak Brahmanandan** · **Maneesha Vinodini Ramesh**
Center for Wireless Networks & Applications (WNA), Amrita Vishwa Vidyapeetham, Amritapuri, India

Cornelia Inauen
Helmholtz Centre for Polar and Marine Research, Alfred Wegener Institute, Potsdam, Germany

Sebastian Uhlemann
Earth and Environmental Sciences Area, Lawrence Berkeley National Laboratory, Berkeley, CA 94720, USA